CHINESE OPTICS LETTERS

Vol. 19, No. 2 | February 2021

Empowering perovskite $PbTiO_3$ nanoparticles with enhanced up-conversion luminescence and thermal sensitivity by introducing Er^{3+} dopant

Jing Zhu (朱 静), Shiqing Xu (徐时清), Lei Lei (雷 磊), Feifei Huang (黄飞飞), and Zhen Xiao (肖 珍)*

Institute of Optoelectronic Materials and Devices, China Jiliang University, Hangzhou 310018, China

*Corresponding author: xiaozhen@cjlu.edu.cn

Received July 2, 2020 | Accepted September 22, 2020 | Posted Online December 10, 2020

Up-convertion (UC) perovskite Er^{3+}-doped $PbTiO_3$ (Er-PTO) nanoparticles with green and red emissions were synthesized via the hydrothermal method. The UC properties were manipulated by adjusting the concentration of Er^{3+} ions dopant. The green emission intensity was decreased as the doping concentration increased from 1% to 4% (mole fraction), whereas the red emission intensity was increased. The influences of Er^{3+} ions on the temperature-sensing performance were further investigated. The results demonstrated that Er-PTO nanoparticles with doping 1% Er^{3+} ions possessed a sensitivity of 3.1×10^{-3} K^{-1} at 475 K, presenting a high potential in optical heating devices.

Keywords: perovskite; $PbTiO_3$; doping; up-conversion; temperature sensor.

DOI: 10.3788/COL202119.021601

1. Introduction

Up-conversion luminescence (UCL) materials with rare earth (RE) ions doping have deserved soaring attention in the past decades because of their excellent properties and potential applications in color displays, temperature sensor devices, drug delivery, photovoltaics, cell imaging, and tumor therapy[1–7]. With the rapid developments in UCL materials, worldwide efforts focus on improving the luminescence emission efficiency, tailoring the color, and extending the applications. Commonly, the emission efficiency and the color of the UCL materials are determined by activators, sensitizers, and crystalline hosts[8]. The activators, including the lanthanide dopants of Tm, Ho, and Er, are the localized luminescent centers that strongly affect the color[9–11]. Meanwhile, the doping concentration has an obvious influence on emission efficiency[11]. To obtain high emission efficiency, a sensitizer (Yb^{3+} ions) is commonly co-doped into UCL hosts along with the activators, because of the sufficient absorption cross section in the near-infrared (NIR) region of the sensitizer[12]. More importantly, in order to achieve high efficiency and a controllable emission profile, the decision of appropriate host materials is also crucial. The up-conversion (UC) host with low phonon energies should provide a crystal field that is suitable for the lanthanide dopant ions[8,13].

Perovskite-type oxides (ABO_3), including $CaTiO_3$, $PbTiO_3$ (PTO), $BaTiO_3$, and $SrTiO_3$, are intensively studied as the host materials[14–19]. On the one hand, the perovskite-type oxides have adjustable crystal structure, and the radii of A-site ions (Ca^{2+}, Pb^{2+}, Ba^{2+}, and Sr^{2+}) and B-site ion of Ti^{4+} are close to the radius of lanthanide ions[20]. Consequently, the introduction of lanthanide ions into the crystal lattice of perovskite oxides has highly practical viability[20]. On the other hand, the perovskite-type oxides have excellent physical properties, chemical stability, and low lattice phonon energies, which are considered to be one of the most promising UC hosts for various applications[18,21,22]. Till now, extensive research activities have been devoted to the rational design and synthesis of UCL materials by employing perovskite oxides as host materials[17,23–25]. For example, owing to the difference in the symmetry of the crystalline structure, the phase transition and the A/B site of Er-doped perovskite $BaTiO_3$ will significantly affect the UCL intensity[17]. Moreover, Mu *et al.* reported that the emission intensity was strongly dependent on the concentration of Yb^{3+} ions in $CaTiO_3$ Yb^{3+}/Er^{3+} nanocubes[14].

As a result of the excellent UCL properties, perovskite-type oxides are also used as temperature sensor materials. Such temperature sensing is a noncontact measurement with high sensitivity, high signal discriminability, and broad range dynamic imaging[16,24,26,27]. In this respect, several literatures have investigated the effects of temperature on the UCL in the RE-doped perovskite-type oxides. Sun *et al.* reported a maximum sensitivity of 1.07×10^{-2} K^{-1} at room temperature for the Er^{3+}, Yb^{3+} co-doped $Ba_{0.8}Sr_{0.2}TiO_3$ ferroelectric ceramics[27]. Meanwhile, Mahata *et al.* demonstrated that Zn^{2+} ions can improve the temperature-sensing performance of the perovskite

$BaTiO_3$ Er^{3+}/Yb^{3+} nanophosphors[16]. Recently, Gong *et al.* verified that the UCL intensity of Er^{3+}-doped PTO (Er-PTO) nanofibers can be modulated by changing the phase structure and polarization intensity of the host materials[15,28]. When the Er^{3+} ions are doped into preperovskite or perovskite PTO nanofibers, due to the differences of substitution sites and chemical environments, the preperovskite one had no UC emission, whereas the perovskite one exhibited green and red emissions. Moreover, the UCL emissions could be modulated by adjusting the tetragonality of the perovskite PTO nanofibers. However, the UC of RE-ions-doped PTO with nanoparticle morphology is rarely reported, as well as the temperature-sensing properties.

Herein, we prepared a series of perovskite Er-PTO nanoparticles with different Er^{3+} doping concentrations by a facile hydrothermal method. The influences of dopant content on the morphology, microstructure, and UC emissions were investigated in detail. When the doping contents increased from 1% to 4% (mole fraction), the intensity of the green emission was decreased, but the intensity of the red one was increased. The maximum integrated intensity ratio of green/red (G/R) was observed at Er^{3+} of 1% concentration. Besides, the effects of Er^{3+} ions on the temperature-sensing performance (333 K to 493 K) were also studied. According to the fluorescence intensity ratio (FIR) technique, PTO materials with the Er^{3+} ions doping concentration of 1% exhibited a maximum sensitivity of $3.1 \times 10^{-3}\ K^{-1}$ at 475 K.

2. Experimental Section

2.1 Synthesis of Er-PTO nanoparticles

Er-PTO (0, 1%, 2%, 3%, and 4%) samples were synthesized by the hydrothermal method. All chemical agents were purchased from Aladdin Chemical Corporation with analytical grade. Firstly, 2.07 g lead nitrate [$Pb(NO_3)_2$] and 0–0.089 g erbium nitrate [$Er(NO_3)_3 \cdot 5H_2O$] were dissolved together in deionized water to form the A solution. Meanwhile, 0.4 g commercial P25 (TiO_2 powder) and 8.4 g potassium hydroxide (KOH) were added into 20 mL deionized water to achieve the B solution. Subsequently, the B solution was individually dropped into the A solution with violent stirring. Then, the obtained precursor suspension was transferred into the autoclave and heat treated at 200°C for 12 h. The resulting products were rinsed with deionized water and ethanol five times and dried in an oven at 60°C for 24 h. The obtained products were named PTO, 1% Er-PTO, 2% Er-PTO, 3% Er-PTO, and 4% Er-PTO for varying Er^{3+} dopant concentrations from 0 to 4%, respectively.

2.2 Characterizations

X-ray diffraction (XRD) patterns were obtained on a Bruker D7 Advance power diffractometer by Cu Kα radiation (λ = 1.54056 Å, 1 Å = 0.1 nm). Scanning electron microscopy (SEM) pictures were collected by a MODEL SU8010 of Hitachi company. Transmission electron microscopy (TEM) results were taken on FEI F20 at a 200 kV accelerating voltage, as well as the high resolution TEM (HRTEM) images. The UC spectra were recorded by a HORIBA PL3-211-P spectrometer. A diode laser with wavelength of 980 nm was used to pump the powders.

3. Results and Discussion

The phase and structure variation of Er-PTO samples are verified by XRD tests. As shown in Fig. 1(a), all of the diffraction peaks of the samples can correspond well to the perovskite PTO (JCPDS 06-0452), as the doping contents of Er^{3+} ions increased from 0 to 4%. Meanwhile, no distinct impurity phase can be detected in Er-PTO samples, implying that the introduced Er^{3+} ions do not alter the pristine structure of PTO. Moreover, in order to reveal the subtle structure changes, the magnified XRD patterns in the 2θ range from 22° to 24° are displayed in Fig. 1(b). Apparently, the (100) peak positions of Er-PTO samples are gradually shifted to higher angles as the Er^{3+} concentration increased from 0 to 2%, whereas the (100) peak positions shift toward the lower angle when the Er^{3+} concentration increases to 3%. By considering the sequence of Shannon effective ionic radii [Ti^{4+}(60.5 pm) < Er^{3+}(100.4 pm) < Pb^{2+}(129 pm)][20], the ionic radius difference between the host and doped one will cause the change of lattice. Therefore, the Er^{3+} ions substituted for the Pb^{2+} ions in the A site may cause shrinkage of the crystal lattices in perovskite PTO. As a result, XRD peaks shift to a higher angle. On the contrary, the replacement of Er^{3+} ions for Ti^{4+} in the B site might lead to the expansion of crystal lattices in perovskite PTO, and hence the peaks shift to a lower angle. As illustrated in Fig. 1(b), the (100) peak positions of Er-PTO samples are gradually shifted to higher angles as the Er^{3+} concentration increases from 0 to 2%, whereas the (100) peak positions shift toward a lower angle when the Er^{3+} concentration increases to 3%. This result indicates that the Er^{3+} doping will cause the lattice expansion at first and then shrinkage. Gong *et al.* reported that Er^{3+} ions could occupy the B site (Ti^{4+}) in perovskite PTO nanofibers by a heat treatment at 650°C in air for 1 h[28]. Moreover, our previous work indicates that Er^{3+} ions can replace the A site in perovskite oxides as well[18]. Consequently, it can be easily inferred that Er^{3+} ions may replace the Pb^{2+} ions first and then the Ti^{4+} ions.

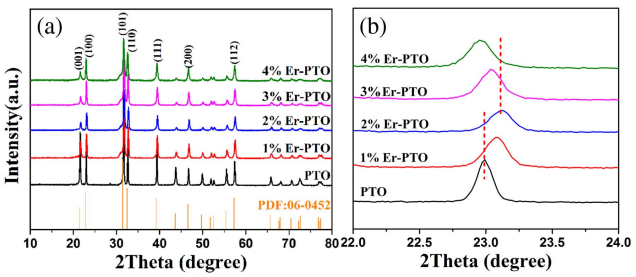

Fig. 1. (a) XRD patterns of Er-PTO nanoparticles. (b) Magnification of (110) diffraction peaks.

The effects of Er^{3+} doping on the morphology and microstructure of Er-PTO samples are observed by SEM. As depicted in Fig. 2(a), the pristine PTO sample exhibits plate-like morphology with a particle size distribution ranging from 0.5 to 2.5 μm. It is worth noting that the Er^{3+} dopant has distinguishable effects on the morphology and particle size of PTO. As shown in Figs. 2(b) and 2(c), the particle size of the Er-PTO sample is reduced significantly along with Er^{3+} doping concentration increasing from 1% to 2%, as well as the morphology of PTO becoming irregular and agglomerated. However, when the Er^{3+} doping concentration increases from 2% to 4% [Figs. 2(c)–2(e)], the particle size changes slightly. This phenomenon could be attributed to the un-equivalent replacement of Pb^{2+} or Ti^{4+} ions by Er^{3+} ions, in which the charge balance is disturbed in PTO. For the purpose of establishing the charge compensation, the vacancies or extra O^{2-} ions need to be introduced into the grain surface[29]. As a result, the diffusion of the crystal nucleus will be hindered, leading to the sluggish growth rate of PTO.

So as to further elucidate the chemical composition and microstructure of Er-PTO samples, TEM, HRTEM, scanning TEM (STEM), and energy dispersive spectroscopy (EDS) elemental mapping results of 1% Er-PTO sample are vividly illustrated in Fig. 3. Obviously, 1% Er-PTO sample has irregular plate-like morphology with a particle size of several hundred nanometers. To get a deep insight into the microstructure of 1% Er-PTO sample, the HRTEM image indicates that 1% Er-PTO sample is highly crystallized since the distinct orderly lattice fringes can be detected in Fig. 3(b). Additionally, the regular lattice fringes have interplanar distances of 0.282 nm and 0.276 nm, which belong to the (101) and (110) lattice planes of perovskite PTO, respectively. According to the STEM and EDS mapping results [Fig. 3(c)], the major elemental signals are Pb, Ti, O, and Er, which is consistent with the chemical composition of 1% Er-PTO sample. Moreover, it should be mentioned that Pb, Ti, O, and Er elemental signals have been detected, and all of them are distributed homogeneously. This result reveals the effective and uniform substitution of Er^{3+} ions in PTO, which would significantly affect the UCL properties.

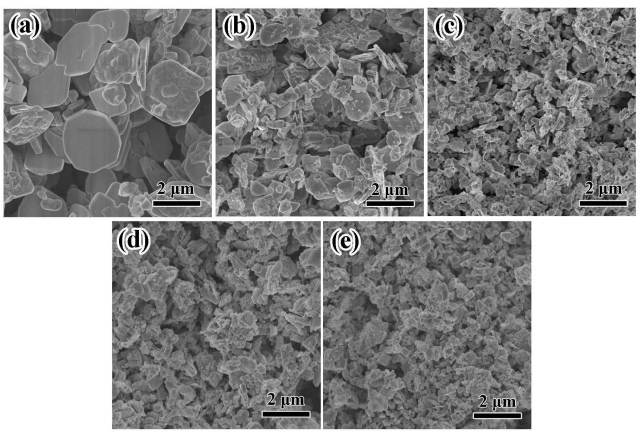

Fig. 2. SEM images of Er-PTO nanoparticles with different Er^{3+} doping concentrations. (a) PTO, (b) 1% Er-PTO, (c) 2% Er-PTO, (d) 3% Er-PTO, (e) 4% Er-PTO, respectively.

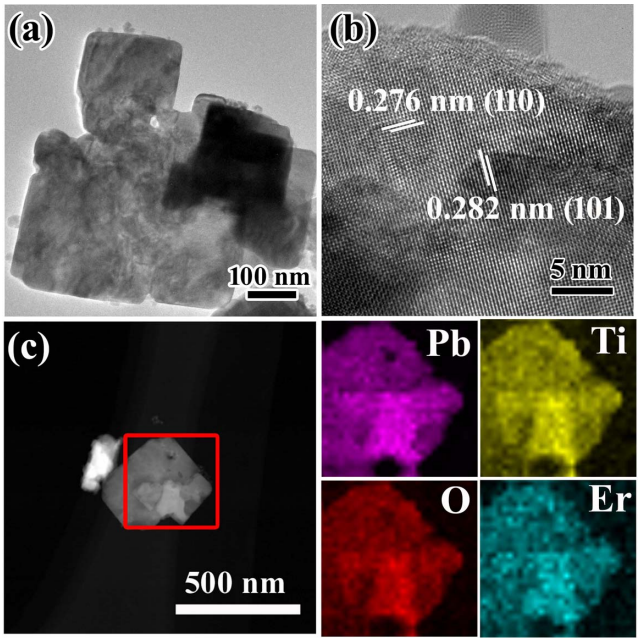

Fig. 3. (a) TEM, (b) HRTEM, and (c) STEM images and the corresponding EDS elemental mapping results of 1% Er-PTO sample.

Figure 4(a) exhibits the UCL spectra of Er-PTO samples with Er^{3+} doping concentration from 0 to 4% at room temperature, which are excited by a diode laser of 980 nm with the power of 500 mW. Apparently, no emission peak exists in the pristine PTO sample, which is similar to our previous work[30]. Interestingly, the UCL spectra of Er-PTO samples have two dominating emissions peaking at the center of 550 nm and 520 nm, originating from $^4S_{3/2}$ and $^2H_{11/2}$ states to $^4I_{15/2}$

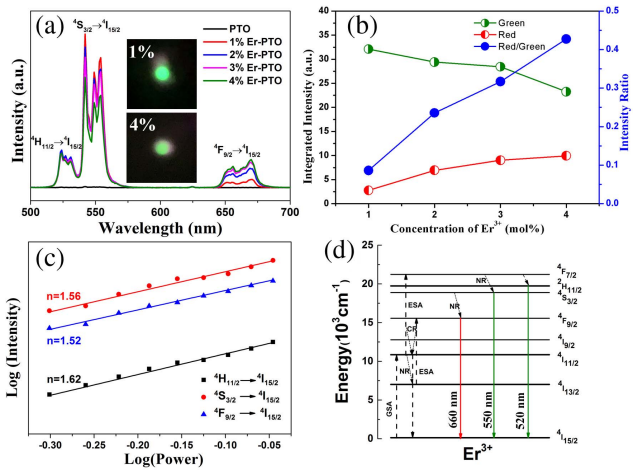

Fig. 4. (a) Room temperature UCL spectra of Er-PTO (0, 1%, 2%, 3%, and 4%). The inset is the digital photographs of the 1% Er-PTO and 4% Er-PTO. (b) Plots of the integrated intensities versus the concentration of Er^{3+} ions. (c) Double logarithmic plots of pump power dependent emission intensities of 1% Er-PTO. (d) Energy levels of Er^{3+} ion and UCL mechanism of Er-PTO crystals.

transitions of Er^{3+} ions. A faint red emission at 660 nm corresponds to the transition from $^4F_{9/2}$ state to $^4I_{15/2}$. In order to intuitively observe the color change of the Er-PTO nanocrystals as the doping concentration increased, the digital photographs of 1% Er-PTO and 4% Er-PTO samples are added into Fig. 4(a). Both samples are green, which could be easily seen by the naked eye. But, the one with dopant content of 1% gets more stable green color output. Additionally, after a careful comparison, the intensity of these UCL emissions strictly depends on the doping concentration of Er^{3+} ions. For the green emission, the integrated intensity is calculated from the range of 515–570 nm, including $^4S_{3/2} \rightarrow {}^4I_{15/2}$ and $^2H_{11/2} \rightarrow {}^4I_{15/2}$ transitions. Meanwhile, the integrated intensity of the red emission centered at 660 nm is calculated from 640 nm to 680 nm. Firstly, we normalized the strength of two parts and then integrated the corresponding area of each part. The integrated intensity of samples and intensity ratio comparisons of red/green have been given in Fig. 4(b). The green emission intensity is gradually decreased as the Er^{3+} concentration increased from 1% to 4%. In contrast, the intensity of the red one is increased slightly. As a result of the loss of intra ions and energy migration, the red/green intensity ratios exhibit an obviously increasing trend when the dopant concentration increased. In fact, the UC emission intensity and color of lanthanide-doped nanocrystals can be modified by controlling the nanocrystal size and the dopant concentration[8]. Generally, the smaller the particle size is, the larger the specific surface area is. Thus, the samples with small particle size will have larger specific surface area along with more surface defects, which may facilitate the non-radiative energy transfer processes and further suppress the UCL. Combined with the SEM and UCL results, the variation of UCL intensity should be attributed to two aspects: one is the particle size, and the other is the doping concentration, but the latter one is dominated. In order to investigate the energy migration process, the pump power dependent emission intensities of 1% Er-PTO phosphors are detected, as displayed in Fig. 4(c). It is worth noting that the UC intensities I of the green emissions centered at 520 nm and 550 nm are calculated from the range of 515–535 nm and 535–570 nm, respectively. The relationship of the UC intensity I and infrared excitation power P for an unsaturated UC process can be calculated by the function of $I \propto P^n$, where n expresses the number of pump photons absorbed per photon emitted, and P is the input laser power. The double logarithmic plots of pump power dependent emission intensities exhibit that the gradients of green and red emissions are 1.56, 1.62, and 1.52, respectively. This result indicates that two photons are employed to populate the $^4S_{3/2} \rightarrow {}^4I_{15/2}$, $^2H_{11/2} \rightarrow {}^4I_{15/2}$, and the $^4F_{9/2} \rightarrow {}^4I_{15/2}$ transitions. However, the values of three slopes are much lower than the theoretical value of two. This could be explained by considering the cross-relaxation process. For example, two ions in $^4F_{9/2}$ level share their energy in such a way that one goes to the $^4S_{3/2}$ level, whereas the other goes to the $^4I_{9/2}$ level. Therefore, a part of the energy of the $^4F_{9/2}$ level is transferred back to the $^4S_{3/2}$ level, leading to the decrease of the slope value. Moreover, due to the pump power in our work ranging from 500 to 900 mW, a formation of heat may happen, and a part of the excitation energy will be lost[16].

To describe the energy transfer mechanisms of UC emissions in the prepared Er-PTO samples, the simplified energy-level diagram is presented in Fig. 4(d). At first, via a ground state absorption (GSA) process, the Er^{3+} ions are excited from the ground state $^4I_{15/2}$ to $^4I_{11/2}$. Subsequently, several extra nuclear electrons of Er^{3+} ions in $^4I_{11/2}$ fall to the $^4I_{13/2}$ level via the non-radiative relaxation (NR) process and then are excited to the $^2F_{9/2}$ state through the GSA process. At the same time, the ions in the $^4I_{11/2}$ level would rise to the $^4F_{7/2}$ level by absorbing another 980 nm photon by an excited state absorption (ESA) process. Then, multiphoton relaxation (MPR) processes occurred, accompanied by NR of electrons to the $^2I_{11/2}$, $^4S_{3/2}$, or $^4I_{9/2}$ levels. Lastly, the electrons in the $^2I_{11/2}$, $^4S_{3/2}$, and $^4I_{9/2}$ levels drop to $^4I_{15/2}$ directly via a radiative process, resulting in the green (520 nm and 550 nm) and red emissions (660 nm).

Generally, temperature plays an important role in the optical properties of UCL materials. As depicted in Fig. 5(a), the UCL spectra of 1% Er-PTO sample excited by 980 nm excitation are obtained with an environment temperature region of 333 K to 493 K. The $^2H_{11/2} \rightarrow {}^4I_{15/2}$ (520 nm) and $^4S_{3/2} \rightarrow {}^4I_{15/2}$ (550 nm) transitions are taken to investigate the sensing characteristic because of the thermal coupling. When the environment temperature rises to 493 K, the luminescence intensity of the 1% Er-PTO sample is reduced sharply, implying that the Er-PTO sample has a highly temperature-sensitive UCL performance.

The integrated intensities ratio of $^2H_{11/2}$ and $^4S_{3/2}$ to $^4I_{15/2}$ transitions for the 1% Er-PTO sample is calculated from temperature-varied emission spectra. As presented in Fig. 5(b), a linear fitting is made for the calculated value of FIR and T. All of the experimental data in Fig. 5(a) were fitted by Eq. (1):

$$\mathrm{FIR} = \frac{I_{520}}{I_{550}} = C \exp\left(\frac{-\Delta E}{kT}\right), \tag{1}$$

in which I_{550} and I_{520} represent the integrated intensities of the $^4S_{3/2} \rightarrow {}^4I_{15/2}$ and $^2H_{11/2} \rightarrow {}^4I_{15/2}$ transitions, respectively; C is a constant; T implies the absolute temperature; k means Boltzmann constant; ΔE is the energy gap between the $^2H_{11/2}$ and $^4S_{3/2}$ levels. ΔE is about 840 cm^{-1}, which could be calculated from the slope of the straight line.

Sensor sensitivity (S) is an essential factor to evaluate the function of the temperature sensors, which is delimited by Eq. (2):

$$S = \frac{d(\mathrm{FIR})}{\mathrm{d}T} = (\mathrm{FIR}) \cdot \frac{\Delta E}{kT}. \tag{2}$$

According to Eq. (2), the sensitivity S is temperature dependent. The maximum senor sensitivity of the 1% Er-PTO sample is defined to be $3.1 \times 10^{-3}\ \mathrm{K}^{-1}$ at 475 K [inset of Fig. 5(b)]. The result is similar to the S of other reported optical materials, especially the RE-doped ferroelectric oxides[16,27,31,32]. These results

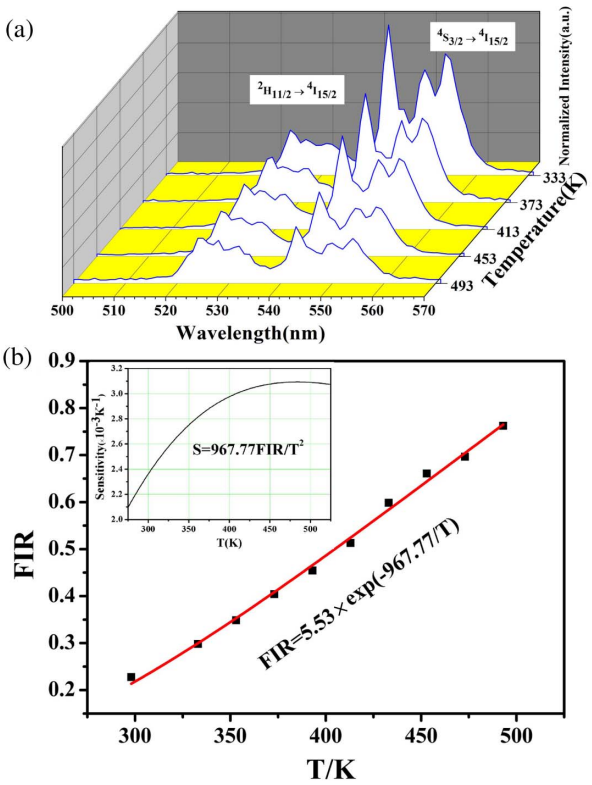

Fig. 5. (a) Fluorescence emission spectra of 1% Er-PTO sample excited by 980 nm excitation with temperature from 333 K to 493 K; (b) temperature-sensing properties for 1% Er-PTO sample. The inset depicts the relationship between sensitivity and absolute temperature.

represent that the Er-PTO particles are good candidates for temperature sensing.

4. Conclusions

In summary, UCL Er-PTO samples without any impurities were prepared by the hydrothermal method. The introduced Er^{3+} ions could replace the Ti^{4+} ions firstly and then the Pb^{2+} ions in PTO. The UCL spectra of Er-PTO phosphors revealed that all of the samples show two strong green emissions and a weak red emission under an excited 980 nm laser, which could originate from the $^4S_{3/2}$, $^2H_{11/2}$, and $^4F_{9/2}$ states to $^4I_{15/2}$ transitions of Er^{3+} ions. Notably, the UC intensities were significantly dependent on the Er^{3+} doping concentration. When the dopant concentration was 1%, the intensity ratio G/R exhibited a maximum value. Moreover, 1% Er-PTO sample has a high sensitivity of $3.1 \times 10^{-3}\ K^{-1}$ at 475 K. The excellent UCL performance and thermal sensitivity of Er-doped ferroelectric materials indicated great potential for multifunctional applications.

Acknowledgement

This work was supported by the Natural Science Foundation of Zhejiang Province (No. LY18E020009).

References

1. C. H. Chen, F. Wang, S. H. Wen, Q. P. Su, M. C. L. Wu, Y. H. Liu, B. M. Wang, D. Li, X. C. Shan, M. Kianinia, I. Aharonovich, M. Toth, S. P. Jackson, P. Xi, and D. Y. Jin, "Multi-photon near-infrared emission saturation nanoscopy using upconversion nanoparticles," Nat. Commun. **9**, 3290 (2018).
2. Z. Wei, H. Ping, D. T. Tu, E. Ma, H. M. Zhu, and X. Y. Chen, "Lanthanide-doped upconversion nano-bioprobes: electronic structures, optical properties, and biodetection," Chem. Soc. Rev. **44**, 1379 (2015).
3. X. J. Zhu, W. Feng, J. Chang, Y. W. Tan, J. C. Li, M. Chen, Y. Sun, and F. Y. Li, "Temperature-feedback upconversion nanocomposite for accurate photothermal therapy at facile temperature," Nat. Commun. **7**, 10437 (2016).
4. Y. J. Liu, Y. Q. Lu, X. S. Yang, X. L. Zheng, S. H. Wen, F. Wang, X. Vidal, J. B. Zhao, D. M. Liu, Z. G. Zhou, C. S. Ma, J. J. Zhou, J. A. Piper, P. Xi, and D. Y. Jin, "Amplified stimulated emission in upconversion nanoparticles for super-resolution nanoscopy," Nature **543**, 229 (2017).
5. S. Chen, A. Z. Weitemier, X. Zeng, L. M. He, X. Y. Wang, Y. Q. Tao, A. J. Y. Huang, Y. Hashimotodani, M. Kano, H. Iwasaki, L. K. Parajuli, S. Okabe, D. B. L. Teh, A. H. All, I. T. Kimura, K. F. Tanaka, and X. G. Liu, "Near-infrared deep brain stimulation via upconversion nanoparticle–mediated optogenetics," Science **359**, 679 (2018).
6. Z. L. Qiu, J. Shu, J. F. Liu, and D. P. Tang, "Dual-channel photoelectrochemical ratiometric aptasensor with up-converting nanocrystals using spatial-resolved technique on homemade 3D printed device," Anal. Chem. **91**, 1260 (2019).
7. J. T. Xu, A. Gulzar, P. P. Yang, H. T. Bi, D. Yang, S. L. Gai, F. He, J. Lin, B. G. Xing, and D. Y. Jin, "Recent advances in near-infrared emitting lanthanide-doped nanoconstructs: Mechanism, design and application for bioimaging," Coordin. Chem. Rev. **381**, 104 (2019).
8. F. Wang and X. G. Liu, "Recent advances in the chemistry of lanthanide-doped upconversion nanocrystals," Chem. Soc. Rev. **38**, 976 (2009).
9. S. Ye, J. Song, D. Wang, Y. L. Tian, J. L. Qu, and H. B. Niu, "Reduced photon quenching in Ce-doped $NaYF_4$:Yb/Ho upconversion nanoparticles with core/shell structure," Chin. Opt. Lett. **14**, 021601 (2016).
10. X. Liu, R. S. Lei, F. F. Huang, D. G. Deng, H. P. Wang, S. L. Zhao, and S. Q. Xu, "Upconversion luminescence, intrinsic optical bistability, and optical thermometry in Ho^{3+}/Yb^{3+}:$BaMoO_4$ phosphors," Chin. Opt. Lett. **17**, 111601 (2019).
11. Y. Kuang, J. T. Xu, C. Wang, T. Y. Li, S. L. Gai, F. He, P. P. Yang, and J. Lin, "Fine-tuning Ho-based red-upconversion luminescence by altering $NaHoF_4$ core size and $NaYbF_4$ shell thickness," Chem. Mater. **31**, 7898 (2019).
12. D. Yan, Z. W. Yang, J. Y. Liao, H. J. Wu, J. B. Qiu, Z. G. Song, D. C. Zhou, Y. Yang, and Z. Y. Ying, "Investigation of the mechanism of upconversion luminescence in Er^{3+}/Yb^{3+} co-doped $Bi2Ti_2O_7$ inverse opal," Chin. Opt. Lett. **11**, 041602 (2013).
13. E. Lu, J. Pichaandi, C. K. Rastogi, L. P. Arnett, and M. A. Winnik, "Influence of cubic-to-hexagonal-phase transformation on the uniformity of $NaLnF_4$ (Ho, Tb, Eu, Sm) nanoparticles," Chem. Mater. **31**, 9742 (2019).
14. J. J. Mu, W. J. Sun, F. Li, Y. Guan, X. M. Zhou, J. Li, and L. Chen, "Upconversion luminescent perovskite $CaTiO_3$:Yb^{3+}/Er^{3+} nanocubes," J. Alloy. Compd. **797**, 1002 (2019).
15. S. Y. Gong, M. Li, Z. H. Ren, X. Yang, X. Li, G. Shen, and G. R. Han, "Polarization-modified upconversion luminescence in Er-doped single-crystal perovskite $PbTiO_3$ nanofibers," J. Phys. Chem. C **119**, 17326 (2015).
16. M. K. Mahata, T. Koppe, T. Mondal, C. Brüesewitz, K. Kumar, V. K. Rai, H. Hofsäss, and U. Vetter, "Incorporation of Zn^{2+} ions into $BaTiO_3$:Er^{3+}/Yb^{3+} nanophosphor: an effective way to enhance upconversion, defect luminescence and temperature sensing," Phys. Chem. Chem. Phys. **17**, 20741 (2015).
17. H. Y. Bae and K. T. Lee, "Effect of tetragonal to cubic phase transition on the upconversion luminescence properties of A/B site erbium-doped perovskite $BaTiO_3$," RSC Adv. **9**, 2451 (2019).
18. Z. Xiao, J. W. Zhang, L. Jin, Y. Xia, L. Lei, H. P. Wang, J. J. Zhang, and S. Q. Xu, "Enhanced up-conversion luminescence intensity in single-crystal $SrTiO_3$:Er^{3+} nanocubes by codoping with Yb^{3+} ions," J. Alloy. Compd. **724**, 139 (2017).
19. L. Xu, R. Q. Zhu, and C. X. Xu, "Broadband photochromic effect and photoluminescence modulation in rare-earth-doped $(Pb,La)(Zr,Ti)O_3$ ceramics," Chin. Opt. Lett. **18**, 091403 (2020).

20. R. D. Shannon, "Revised effective ionic radii and systematic studies of interatomic distances in halides and chalcogenides," Acta Cryst. **A32**, 751 (1976).
21. X. Li, Y. Li, X. Chen, B. Li, B. Gao, Z. Ren, G. Han, and C. Mao, "Optically monitoring mineralization and demineralization on photoluminescent bioactive nano-fibers," Langmuir **32**, 3226 (2016).
22. L. Meng, K. Zhang, K. Pan, Y. Qu, and G. Wang, "Controlled synthesis of $CaTiO_3$:Ln^{3+} nanocrystals for luminescence and photocatalytic hydrogen production," RSC Adv. **6**, 5761 (2016).
23. S. F. Liu, H. Ming, J. Cui, S. B. Liu, W. X. You, X. Y. Ye, Y. M. Yang, H. P. Nie, and R. X. Wang, "Color-tunable upconversion luminescence and multiple temperature sensing and optical heating properties of $Ba_3Y_4O_9$:Er^{3+}/Yb^{3+} phosphors," J. Phys. Chem. C **122**, 16289 (2018).
24. J. J. Mu, C. Y. He, W. J. Sun, Y. Guan, J. Li, J. Li, X. M. Zhou, and L. Chen, "Zn^{2+}-improved upconversion luminescence of perovskite nanophosphors," Mater. Res. Bull. **121**, 110610 (2020).
25. G. Kim, S. J. Lee, and Y. J. Kim, "The effects of zinc on the structural and luminescent properties of $Ca_{1-x}Zn_xTiO_3$:Pr^{3+} phosphors," Opt. Mater. **34**, 1860 (2012).
26. A. G. He, Z. Z. Xi, X. J. Li, W. Long, P. Y. Fang, and J. Zhang, "Temperature dependence of upconversion luminescence and sensing sensitivity of Ho^{3+}/Yb^{3+} modified PSN-PMN-PT crystals," J. Alloy. Compd. **803**, 450 (2019).
27. Q. Sun, W. H. Wang, Y. X. Pan, Z. K. Liu, X. Q. Chen, and M. Ye, "Effects of temperature and electric field on upconversion luminescence in Er^{3+}-Yb^{3+} codoped $Ba_{0.8}Sr_{0.2}TiO_3$ ferroelectric ceramics," J. Am. Ceram. Soc. **100**, 4661 (2017).
28. S. Y. Gong, Z. H. Ren, S. Jiang, M. Li, X. Li, X. Wei, G. Xu, G. Shen, and G. R. Han, "Phase-modified up-conversion luminescence in Er-doped single-crystal $PbTiO_3$ nanofibers," J. Phys. Chem. C **118**, 5486 (2014).
29. S. Jiang, P. Zeng, L. Q. Liao, S. F. Tian, H. Guo, Y. H. Chen, C. K. Duan, and M. Yin, "Optical thermometry based on upconverted luminescence in transparent glass ceramics containing $NaYF_4$:Yb^{3+}/Er^{3+} nanocrystals," J. Alloy. Compd. **617**, 538 (2014).
30. Z. Xiao, J. W. Zhang, J. Zhu, H. Xu, H. P. Wang, S. Xu, and Y. Xia, "Hydrothermal synthesis and up-conversion luminescence of Ho^{3+}/Yb^{3+} co-doped $PbTiO_3$," Z. Anorg. Allg. Chem. **645**, 1111 (2019).
31. P. Du, L. H. Luo, X. Y. Huang, and J. S. Yu, "Ultrafast synthesis of bifunctional Er^{3+}/Yb^{3+}-codoped $NaBiF_4$ upconverting nanoparticles for nanothermometer and optical heater," Colloid Interface Sci. **514**, 172 (2018).
32. P. Du, L. H. Luo, W. P. Li, and Q. Y. Yue, "Upconversion emission in Er-doped and Er/Yb-codoped ferroelectric $Na_{0.5}Bi_{0.5}TiO_3$ and its temperature sensing application," J. Appl. Phys. **116**, 014102 (2014).